COMPUTATION OF FLOW IN A COMPRESSOR BLADE ROW BY A THIRD-ORDER ACCURATE HIGH-RESOLUTION SCHEME

Jixian Yao*
University of California, Irvine, Irvine, CA92697
Xinhai Zhou†
Northwestern Polytechnical University, Xian, China

Abstract

The three dimensional transonic flow field inside an isolated compressor blade row is calculated by using a third order accurate essentially nonoscillatory scheme (ENO3). The complexity of ENO3 scheme results in extra computational work, so the lower-upper symmetric Gauss-Seidel algorithm (LU-SGS) is adopted to improve the computational efficiency. NASA Lewis Rotor37 has been used as a test case. Detailed comparisons between calculation and measurement, including overall performance, shock wave system, and downstream wake, are carried out to show the resolving capability of this solver.

1 Introduction

The flows in transonic axial compressor and fan rotor blade rows are very complex, which include three dimensional shocks, tip leakage flows, endwall and blade surface boundary layers and other complex secondary flows. Shock structure and shock interaction with boundary layers are the key factors that affect the performance and stability of rotors. Therefore, detailed numerical simulation of shocked flows is essential to the design of modern high performance compressors. In order to improve the resolving quality for the shape and position of shock waves, A third order accurate, essentially nonoscillatory scheme (ENO3) developed by J. Y. Yang[1] is employed.

The original ENO3 scheme is third order in both time and space. For steady flow calculation, we are only interested in the accuracy in space, Consequently, the scheme is simplified to retain third order accuracy in space but only first-order in time.

Compared to TVD schemes, ENO schemes can retain the same spatial accuracy at extremal points where TVD schemes reduce to first-order. In addition, a third-order accurate ENO scheme may help resolve viscous boundary layer since the numerical dissipation due to truncation is in the form of 4-th order derivatives which is higher than the physical viscous terms in the form of second-order derivatives.

On the other hand, the spatial discretization stencil of the ENO3 scheme involves 7 mesh nodes in one direction, and the scheme itself is also more complex including Jacobian evaluation and matrix manipulation. This results in extra computational work and affects the efficiency to reach steady state. To overcome this problem, the lower-upper symmetric Gauss-Seidel (LU-SGS) algorithm developed by Yoon and Jameson[2], which avoids any matrix inverse operations and still preserves stability in three dimensions, is used for steady calculations. Because the time step can be set to infinity, the computational efficiency is greatly improved.

The NASA Lewis Rotor37 is calculated as a test example and compared with the experimental data. The comparison includes the overall performance, the shock wave system, and the wake.

2 Governing Equations

The Reynolds-averaged Navier-Stokes equations used in this paper take the absolute velocity as the conservative variables. This is convenient for inflow boundary condition treatment and its eigen system deduction. The equations in relative cylindrical coordinates (θ, r, z) can be written for generalized curvilinear coordinates (ξ, η, ζ) fixed to blade as follows:

$$\frac{\partial Q}{\partial t} + \frac{\partial E}{\partial \xi} + \frac{\partial F}{\partial \eta} + \frac{\partial G}{\partial \zeta} = K + \frac{\partial E_v}{\partial \xi} + \frac{\partial F_v}{\partial \eta} + \frac{\partial G_v}{\partial \zeta} \quad (1)$$

*Postdoctoral Fellow, Department of Mechanical and Aerospace Engineering, Member AIAA, Current Address: Dept. of Aeronautics and Astronautics, Stanford University

†Professor, Department of Aeroengine, Northwestern Polytechnical University

where

$$Q = J^{-1}\begin{bmatrix} r\rho \\ r\rho u \\ r\rho v \\ r\rho w \\ re \end{bmatrix}$$

$$E,F,G = J^{-1}\begin{bmatrix} r\rho\Theta_k \\ r\rho u\Theta_k + rpk_\theta/r \\ r\rho v\Theta_k + rpk_r \\ r\rho w\Theta_k + rpk_z \\ r\Theta_k(e+p) + \omega r^2 pk_\theta/r \end{bmatrix}$$

$$K = J^{-1}\begin{bmatrix} 0 \\ -\rho uv + \tau_{\theta r} \\ \rho u^2 + p - \tau_{\theta\theta} \\ 0 \\ 0 \end{bmatrix}$$

$$E_v,F_v,G_v = J^{-1}\begin{bmatrix} 0 \\ \tau_{\theta\theta}k_\theta + r\tau_{\theta r}k_r + r\tau_{\theta z}k_z \\ \tau_{r\theta}k_\theta + r\tau_{rr}k_r + r\tau_{rz}k_z \\ \tau_{z\theta}k_\theta + r\tau_{zr}k_r + r\tau_{zz}k_z \\ T_\theta k_\theta + rT_r k_r + rT_z k_z \end{bmatrix}$$

$$k = \xi,\eta,\zeta$$

where

$$\Theta_k = (u-\omega r)k_\theta/r + vk_r + wk_z$$

$$T_\theta = \tau_{\theta\theta}u + \tau_{\theta r}v + \tau_{\theta z}w - q_\theta$$

$$T_r = \tau_{r\theta}u + \tau_{rr}v + \tau_{rz}w - q_r$$

$$T_z = \tau_{z\theta}u + \tau_{zr}v + \tau_{zz}w - q_z$$

$$\tau_{\theta\theta} = \frac{2}{3}(\mu+\mu_t)[2\frac{\partial u}{r\partial\theta} - \frac{\partial v}{\partial r} - \frac{\partial w}{\partial z} + 2\frac{v}{r}]$$

$$\tau_{rr} = \frac{2}{3}(\mu+\mu_t)[2\frac{\partial v}{\partial r} - \frac{\partial u}{r\partial\theta} - \frac{\partial w}{\partial z} - \frac{v}{r}]$$

$$\tau_{zz} = \frac{2}{3}(\mu+\mu_t)[2\frac{\partial w}{\partial z} - \frac{\partial u}{r\partial\theta} - \frac{\partial v}{\partial r} - \frac{v}{r}]$$

$$\tau_{\theta r} = \tau_{r\theta} = (\mu+\mu_t)[\frac{\partial u}{\partial r} + \frac{\partial v}{r\partial\theta} - \frac{u}{r}]$$

$$\tau_{rz} = \tau_{zr} = (\mu+\mu_t)[\frac{\partial v}{\partial z} + \frac{\partial w}{\partial r}]$$

$$\tau_{\theta z} = \tau_{z\theta} = (\mu+\mu_t)[\frac{\partial w}{r\partial\theta} + \frac{\partial u}{\partial z}]$$

$$q_\theta = -Cp(\frac{\mu}{\mathrm{Pr}} + \frac{\mu_t}{\mathrm{Pr_t}}\frac{\partial T}{r\partial\theta})$$

$$q_r = -Cp(\frac{\mu}{\mathrm{Pr}} + \frac{\mu_t}{\mathrm{Pr_t}}\frac{\partial T}{\partial r})$$

$$q_z = -Cp(\frac{\mu}{\mathrm{Pr}} + \frac{\mu_t}{\mathrm{Pr_t}}\frac{\partial T}{\partial z})$$

where ρ is the density; u, v, and w are the absolute components of velocity in (θ, r, z) directions respectively; e is total internal energy; T is static temperature; ω is angular velocity; pressure $p = (\gamma-1)[e - \rho(u^2+v^2+w^2)/2]$; γ is the specific heat ratio; J is metric Jacobian; τ and q are the shear stress tensor and heat flux vector, respectively; Pr and $\mathrm{Pr_t}$ are the molecular and turbulent Prandtl number; Cp is the specific heat of constant pressure. μ and μ_t are the molecular and turbulent eddy viscosity, which are evaluated by Sutherland's formula and the Baldwin-Lomax algebraic turbulence model.

3 Numerical Scheme ENO3

The ENO3 scheme with first-order time accuracy and third-order space accuracy used in this paper is described in Ref.[4]. For the convection term in ξ direction, the space discretization is as follows:

$$\frac{\partial E}{\partial\xi} = \hat{A}^+\Delta_- E_i^M + \hat{A}^-\Delta_+ E_i^M$$

where the modified vector is

$$E_i^M = E_i + C_i + D_i$$

the components of the additional vector C_i are

$$c_i^l = \mathrm{minmod}(\tilde{c}^l_{i-\frac{1}{2}}, \tilde{c}^l_{i+\frac{1}{2}})$$

where $\tilde{c}^l_{i+\frac{1}{2}}$ is the components of the following vector:

$$\tilde{C}_{i+\frac{1}{2}} = \mathrm{sgn}A_{i+\frac{1}{2}}\Delta_{i+\frac{1}{2}}E/2$$

the components of the additional vector D_i are

$$d_i^l = \begin{cases} \bar{\mathrm{m}}(\Delta_-\tilde{d}^l_{i-\frac{1}{2}}, \Delta_+\tilde{d}^l_{i-\frac{1}{2}}) & \text{if} \left|\Delta_{i-\frac{1}{2}}q^l\right| \le \left|\Delta_{i+\frac{1}{2}}q^l\right| \\ \bar{\mathrm{m}}(\Delta_-\hat{d}^l_{i+\frac{1}{2}}, \Delta_+\hat{d}^l_{i+\frac{1}{2}}) & \end{cases}$$

where $\tilde{d}^l_{i+\frac{1}{2}}$ and $\hat{d}^l_{i+\frac{1}{2}}$ are the components of the following vectors, respectively.

$$\tilde{D}_{i+\frac{1}{2}} = \mathrm{sgn}A_{i+\frac{1}{2}}\Delta_{i+\frac{1}{2}}E/3$$

$$\hat{D}_{i+\frac{1}{2}} = -\mathrm{sgn}A_{i+\frac{1}{2}}\Delta_{i+\frac{1}{2}}E/6$$

A is the coefficient Jacobian in ξ direction, and

$$\mathrm{sgn}A = R\,\mathrm{diag}\{\mathrm{sgn}(a_l)\}\,L$$

$$\hat{A}^\pm = R\,\mathrm{diag}\{\hat{a}_l^\pm\}\,L$$

$$\hat{a}_l^\pm = (1 \pm \mathrm{sgn}a_l)/2$$

where L and R are the left and right eigen matrices, respectively, a_l are the eigen values of A, $l = 1 \sim 5$.

$$\bar{\mathrm{m}}(a,b) = \begin{cases} a & \text{if } |a| \leq |b| \\ b & \end{cases}$$

$$\mathrm{minmod}(a,b) = \begin{cases} s \min(|a|,|b|) & \text{if sgn}a = \text{sgn}b = s \\ 0 & \end{cases}$$

Similar expressions can be written for η and ζ directions. Central difference is used for discretizing viscous terms.

4 LU-SGS Algorithm and Boundary Conditions

The implicit scheme of Eq.(1) can be written in delta form:

$$\begin{aligned}[\frac{I}{\Delta t} + (\Delta_- A^+ + \Delta_- B^+ + \Delta_- C^+) + \\ (\Delta_+ A^- + \Delta_+ B^- + \Delta_+ C^-)]\delta Q = R\end{aligned} \tag{2}$$

where R is the right-hand-side explicit part evaluated by the above techniques. A, B, C are the coefficient Jacobians in ξ, η, ζ directions, and

$$A^{\pm} = (A \pm r_A I)/2$$
$$B^{\pm} = (B \pm r_B I)/2$$
$$C^{\pm} = (C \pm r_C I)/2$$

where r_A, r_B, r_C are the spectral radii of $A, B, andC$. when $\Delta t \to \infty$, Eq.(2) can be written as:

$$\begin{aligned}[\Delta_- A^+ + \Delta_- B^+ + \Delta_- C^+ + \\ \Delta_+ A^- + \Delta_+ B^- + \Delta_+ C^-]\delta Q = R\end{aligned} \tag{3}$$

The LU decomposition of Eq.(3) is

$$L\, D^{-1}\, U\, \delta Q = R$$

where

$$L = r_{ABC} I - A^+_{i-1} - B^+_{j-1} - C^+_{k-1}$$
$$D = r_{ABC} I$$
$$U = r_{ABC} I + A^-_{i+1} + B^-_{j+1} + C^-_{k+1}$$
$$r_{ABC} = r_A + r_B + r_C$$

The solution procedure is
L-operator:

$$\delta Q^* = (R + A^+_{i-1}\delta Q^*_{i-1} + B^+_{j-1}\delta Q^*_{j-1} + C^+_{k-1}\delta Q^*_{k-1}) / r_{ABC}$$

U-operator:

$$\delta Q = \delta Q^* - (A^+_{i+1}\delta Q^*_{i+1} + B^+_{j+1}\delta Q^*_{j+1} + C^+_{k+1}\delta Q^*_{k+1}) / r_{ABC}$$

Update:

$$Q^{n+1} = Q^n + \delta Q$$

For inflow condition, total pressure, total temperature, tangential velocity, and radial velocity are fixed. For outflow condition, the tip back pressure is fixed and the radial equilibrium equation is introduced. The parameters for outflow boundary should be carefully handled, the characteristic relations are employed in the calculation.

5 Results and Discussion

NASA Lewis Rotor37 is used as a test case to validate the solver. The rotor has 36 blades, rotating speed is 171887 rpm. Tip wheel speed is 454.14 m/s. The whole inflow plane is supersonic. The computational grid is $49 \times 49 \times 85$ (tangential$\times$radial$\times$axial) as shown in Figure 1. The first grid spacing near solid wall is set to 0.0002 of blade chord. The operating point of M/M_{choke}=0.98 is calculated. The comparisons include the distribution of overall performance parameters, shock system, and wakes.

In order to reveal the improvement of the third order accurate scheme, a calculation using the same grid but second order TVD scheme(NND[5]) has been performed. Figure 2 shows the Mach number distribution in blade-to-blade direction at mid-span and 20% chord from the leading edge of Rotor37 blade. It indicates that the ENO3 scheme gives better prediction of the boundary layer velocity profile.

Figure 3 is spanwise distribution of adiabatic efficiency. Predicted efficiency agrees well with measured values over almost the whole span. The distribution of total pressure ratio is shown in Figure 4. The variation trend of predicted and measured values are generally the same. The difference becomes larger near hub and tip. The comparison of the exit absolute angles is shown in Figure 5. Computed angles are in very good agreement with the measurement at almost the whole span. The differences are in 2 degrees except near endwalls.

The comparisons of shock system are shown in Figure 6 and Figure 7. Figure 6 and Figure 7 are the blade-to-blade relative Mach number at 20% chord from leading edge at 50% span and 90% span respectively. The predicted peak values and shapes coincide with the experiment at two different spanwise positions. However, the predicted Mach number behind the shocks is slightly lower than that from the experiment. Figure 6 and Figure 7 also indicate that, the computed end position of shocks agree with the experiment, however, as shown in Figure 6 and Figure 7, computed Mach numbers drop down ahead of the measured shock wave front position. This situation is more obvious at mid-span where the shock is relatively weak, whereas for the strong shock at 90% span, the predicted shock becomes thinner. This probably is the essential feature of dissipative-type shock-capturing schemes.

Figure 8 gives the tangential Mach number at 50% span immediately downstream of the blade trailing edge. Predicted wake shape and wake width are very similar to those measured in the experiment. Figure 9 is the tangential Mach number at exit mid-span. At the position far away from the blade, the solver can still predict the wake distribution well. Except that the predicted width is slightly larger than the experiment, the predicted maximum and minimum Mach numbers agree well with the measurement.

6 Concluding Remarks

A third-order accurate ENO scheme with an implicit LU-SGS time-stepping method is developed for predicting viscous flows in a turbomachinery blade row. The method is used to calculate the flow of the NASA Lewis Rotor37 test case. The computation provides good resolution of the shock system and the wakes in flow. The computed performance parameters agree well with the experimental data.

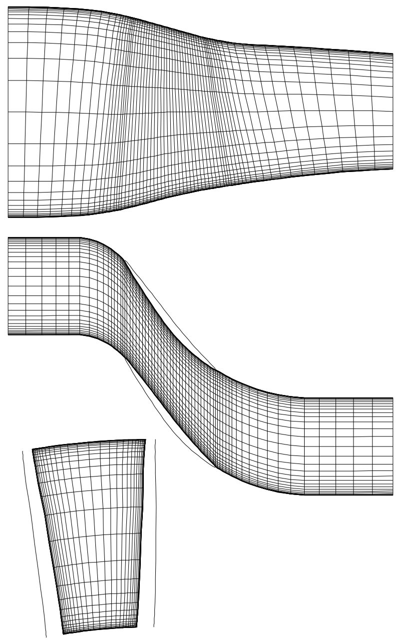

Figure 1: Computational mesh of Rotor37

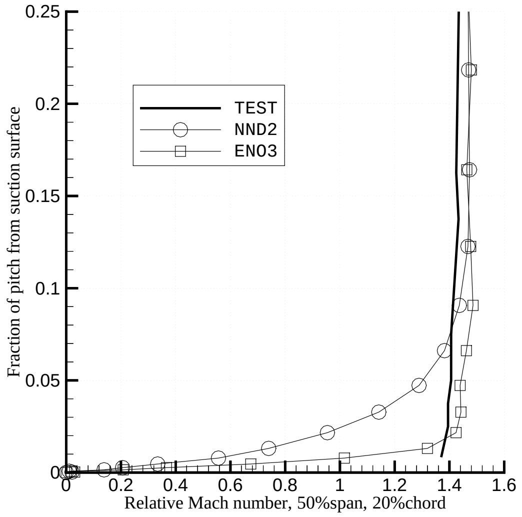

Figure 2: The calibration of numerical schemes

References

[1] J. Y. Yang, "Third Order Nonoscillatory Schemes for the Euler Equations", AIAA J., Vol.29, No.10, 1991

[2] S. Yoon, A. Jameson, "Lower-Upper Symmetric Gauss-Seidel Method for the Euler and Navier-Stokes Equations", AIAA J., Vol.26, No.9, 1988

[3] A. Harten, "High Resolution Scheme for Hyperbolic Conservation Laws", J. of Comp. Phys., Vol.49, No.3

[4] J. Yao, "Numerical Simulation of Transonic Compressor Flow and Shock Wave Control", Ph.D dissertation, Northwestern Polytechnical University, 1995

[5] H. Zhang, "Nonoscillatory, Non-free-parameter, Dissipative Schemes", ACTA AERODYNAMICA SINICA, Vol.6, No.2, 1988

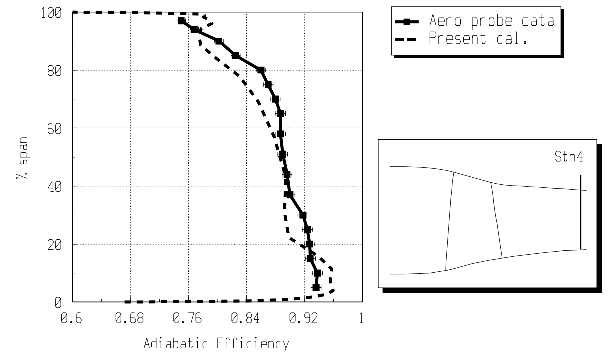

Figure 3: Spanwise variation of adiabatic efficiency, $M/M_{choke} = 0.98$

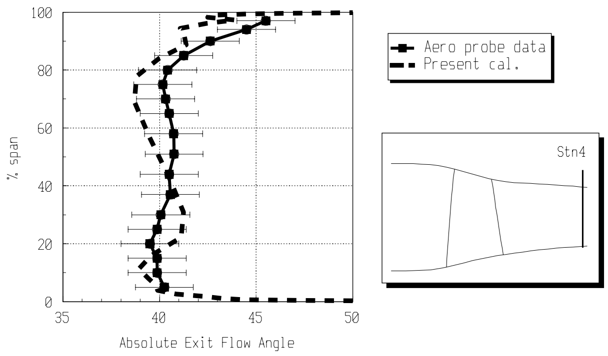

Figure 5: Spanwise variation of absolute flow angle, $M/M_{choke} = 0.98$

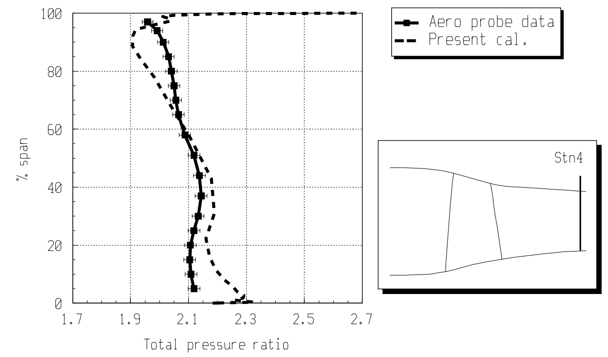

Figure 4: Spanwise variation of total pressure ratio, $M/M_{choke} = 0.98$

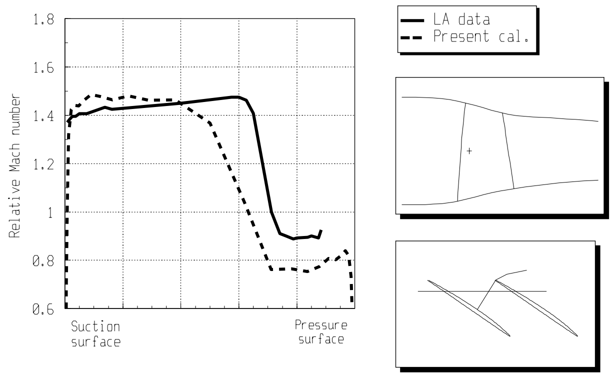

Figure 6: Blade-to-blade relative Mach number at 20% chord and 50% span, $M/M_{choke} = 0.98$

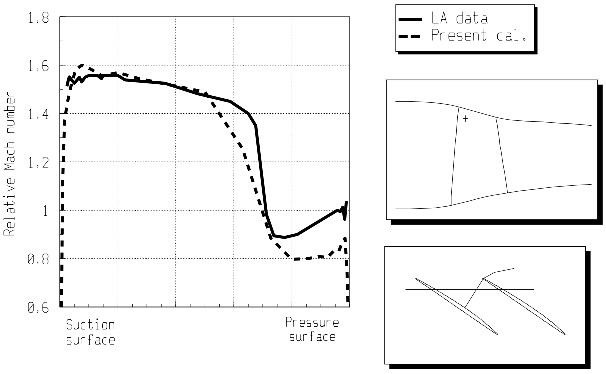

Figure 7: Blade-to-blade relative Mach number at 20% chord and 90% span, $M/M_{choke} = 0.98$

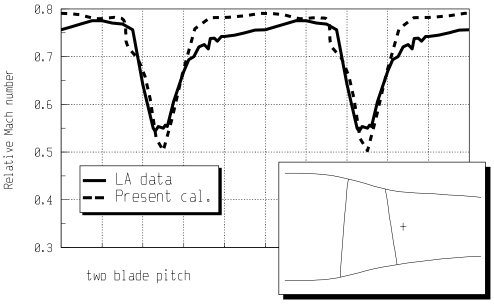

Figure 8: Relative Mach number at 50% span and downstream the trailing edge , $M/M_{choke} = 0.98$

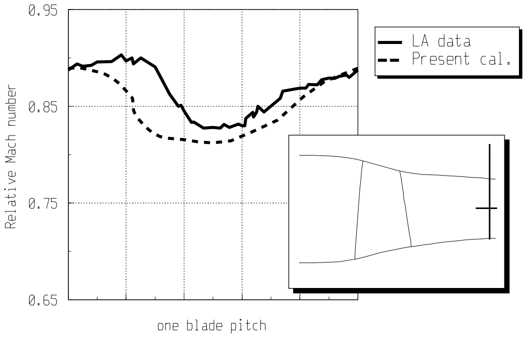

Figure 9: Relative Mach number at 50% span and exit, $M/M_{choke} = 0.98$